OPEN ACCESS

University of Dundee

University of Dundee

Alloyed AuFeZnSe quantum dots@gold nanorod nanocomposite as an ultrasensitive and selective plasmon-amplified fluorescence OFF-ON aptasensor for arsenic (III)

Adegoke, Oluwasesan; Nic Daeid, Niamh

Published in:
Journal of Photochemistry and Photobiology A: Chemistry

DOI:
10.1016/j.jphotochem.2021.113755

Publication date:
2022

Licence:
CC BY-NC-ND

Document Version
Peer reviewed version

Link to publication in Discovery Research Portal

Citation for published version (APA):
Adegoke, O., & Nic Daeid, N. (2022). Alloyed AuFeZnSe quantum dots@gold nanorod nanocomposite as an ultrasensitive and selective plasmon-amplified fluorescence OFF-ON aptasensor for arsenic (III). *Journal of Photochemistry and Photobiology A: Chemistry*, *426*, Article 113755. Advance online publication. https://doi.org/10.1016/j.jphotochem.2021.113755

General rights
Copyright and moral rights for the publications made accessible in Discovery Research Portal are retained by the authors and/or other copyright owners and it is a condition of accessing publications that users recognise and abide by the legal requirements associated with these rights.

• Users may download and print one copy of any publication from Discovery Research Portal for the purpose of private study or research.
• You may not further distribute the material or use it for any profit-making activity or commercial gain.
• You may freely distribute the URL identifying the publication in the public portal.

Take down policy
If you believe that this document breaches copyright please contact us providing details, and we will remove access to the work immediately and investigate your claim.

Download date: 30. Sep. 2023

Alloyed AuFeZnSe quantum dots@gold nanorod nanocomposite as an ultrasensitive and selective plasmon-amplified fluorescence OFF-ON aptasensor for arsenic (III)

Oluwasesan Adegoke*, Niamh Nic Daeid

Leverhulme Research Centre for Forensic Science, School of Science & Engineering, University of Dundee, Dundee, DD1 4GH, UK

* Correspondence: o.adegoke@dundee.ac.uk.
Leverhulme Research Centre for Forensic Science, School of Science & Engineering, University of Dundee, Dundee, DD1 4GH, UK

ABSTRACT

According to documented reports, more than 200 million people across the globe are exposed to arsenic (As) contamination at levels above the World Health Organization (WHO) guideline limit of 10 µg/L. In this work, a novel fluorescence OFF-ON ultrasensitive aptasensor was developed for As (III). To construct the fluorescence aptasensor, AuFeZnSe alloyed quantum dots (QDs) were newly synthesized and surface-coated with amphiphilic polymers (Amp-P) to render the QDs biocompatible and stable. Thereafter, cationic gold nanorods (AuNRs) were electrostatically bonded to the Amp-P-QDs to form an Amp-P-QDs-AuNR nanocomposite which switched OFF the fluorescence of the bound QDs. Thiolated anti-As (III) DNA aptamer (Apt) was thereafter assembled on the Amp-P-QDs-AuNR surface to form a Amp-P-Apt-QDs-AuNR probe. The affinity binding interaction between the targeted As (III) concentration and the Apt, triggered localized surface plasmon resonance (LSPR) from AuNRs to amplify the fluorescence intensity signal, thereby switching ON the fluorescence of the bound Amp-P-QDs. Comparison of the Amp-P-Apt-QDs and the Amp-P-Apt-QDs-AuNR probes, showed that the presence of AuNR enhanced the fluorescence of the bound Amp-P-QDs for As (III) by as much as 230%, representing an ~20-fold increase over the Amp-P-Apt-QDs probe without AuNRs. Under optimum conditions, As (III) was selectively and quantitatively detected with ultra-high sensitivity. The linear range was 0.01 -100 µg/L, while the obtained detection limit of 0.01 µg/L (69.12 pM) was 1000 times lower than the WHO recommended limit. We successfully applied the Amp-P-Apt-QDs-AuNR probe to detect As (III) in environmental and biological samples with analytical recoveries from ~ 93-105%.

1. Introduction

Arsenic is a well-known carcinogen and also widely known to affect more than 200 million people worldwide exposed to arsenic contaminated groundwater that is well beyond the permissible limit of 10 µg/L recommended by the World Health Organisation (WHO) **[1-9]**. Within the environment, arsenic exist in various inorganic forms such as arsine (-3 in AsH_3), arsenite (+3 in AsO_2^-, AsO_3^{3-}), elemental arsenic (0), and arsenate (+5 in AsO_4^{3-}) **[10,11]**. Amongst the different oxidized forms of arsenic, trivalent arsenic (As (III), arsenite), found in reduced atmospheres, and pentavalent arsenic (As (V), arsenate), prevalent in oxygenated environments, are the two major species present in natural water, specifically ground water **[5,12]**. According to the chemical environment assessment, the ratio of As (III) to As (IV) was found to be in the range of 100 to 10 **[13]**. Hence, As (III) is known to be more prevalent in the environment and has been reported to be 25 - 60 times more harmful to humans than As (V) **[14]**. The presence of arsenic in groundwater poses serious threat to humans, animals, and plants alike. Its presence can induce both acute and chronic toxicity to humans leading to abdominal pain, hair loss, weight loss, reflex losses, dyspepsia, anorexia, colitis, gastritis, and respiratory problems **[15,16]**.

In the past three decades, there have been several instrumental techniques and chemical methods that have been developed for As. Molybdenum blue **[17]**, silver diethyldithiocarbamate, and the **[18]** Gutzeit test, **[19]** are the three most commonly used colorimetric chemical methods for arsenic recognition. These methods, though common, are not overly selective to arsenic and their limit of detection (LOD) does not meet the WHO's recommended limit for arsenic recognition **[20]**. Also, AsH_3 hypertoxic gas is released in both the silver diethyldithiocarbamate and Gutzeit test, thus posing serious threat to users and the environment alike **[20]**. In terms of instrumental methods used in arsenic detection, inductively coupled plasmo-mass spectrometry, atomic emission spectroscopy, atomic fluorescence spectroscopy and atomic absorption spectroscopy are the most popular **[20]**. Common limitations of the chemical method such as low sensitivity and low LOD are circumvented using these analytical techniques. However, the high cost of the instrumentation, prolonged analysis time, and the need for highly skilled personnel to operate the instrument, limits their use for on-site arsenic monitoring.

To circumvent the shortcomings of traditional colorimetric and instrumental methods for arsenic detection, affinity-based optical biosensors using nanomaterials as nanocarriers or signal transducers have drawn significant interest within the past decade **[21,22]**. The unique possibility of detecting ultralow concentrations of an analyte in various matrices, the ability to selectively detect the target analyte without interferences, the robust flexibility for assay development, and the ability to transform the sensor into a miniaturised portable hand-held point-of-use detection device, has triggered a huge surge in mainstream nanobiosensor research.

Amongst the various affinity-based biosensor concepts, aptamer (Apt)-based nanobiosensors have drawn significant interest **[23].** The flexible conformational structures of Apts which allow it to fold into secondary and tertiary helical structures have been the basis for selective binding to a target

analyte with high affinity **[24]**. The biomolecular Apt-analyte binding interaction has been exploited on various nanomaterials surfaces to construct aptasensors for various analytes such as small molecules **[25]**, ions **[26]**, proteins **[27]**, peptides **[28]**, and tissues **[29]**, etc. Hence, there is a continued interest in the use of Apt technology for the construction of affinity-based nanobiosensor devices.

Amongst the various aptasensor transduction platform, fluorescence aptasensor has drawn considerable interest. The large surface area, size-dependent optical properties, narrow emission spectra, broad absorption, and excellent photostability of nano-fluorophores such as semiconductor quantum dots (QDs) nanocrystals have drawn huge interest over the past two decades **[30]**. Particularly, QDs aptasensor for As (III) have been reported in the literature **[31,32]**. However, there is still a considerable interest in the development of novel QD-based fluorescence aptasensor for arsenic exhibiting improved sensitivity and versatile applicability. Exploiting the optical properties of QDs by modifying their surfaces with other nanomaterial to form hybrid nanostructured systems, represents a unique and versatile means to develop highly sensitive, highly selective and rapid sensor detection systems.

In this work, we report on the construction of a novel fluorescence aptasensor for As (III) using hybrid nanocomposite of non-cadmium containing amphiphilic polymer (Amp-P)-coated AuFeZnSe alloyed QDs and gold nanorods (AuNRs). Novel AuFeZnSe alloyed QDs were synthesized and used as the choice fluorophore signal reporter for this work, rather than the commonly used cadmium-based Group II-VII fluorescent QDs that may pose safety risk concern. Hydrophobic AuFeZnSe QDs were synthesized via the hot injection organometallic pyrolysis of metal precursors, surfactants, and organic ligands and were transformed into hydrophilic QD nanocrystals via Amp-p coating. Cationic AuNRs were synthesized via the seed-mediated approach and coated with cetyltrimethyl ammonium bromide (CTAB). Electrostatic interaction formed between the Amp-P-coated AuFeZnSe QDs and CTAB-AuNRs, switched OFF the fluorescence of the bound QDs. However, based on the binding affinity between the aptamer and the targeted As (III) concentration, the fluorescence of the QDs was switched ON with enhanced fluorescence intensity via localized surface plasmon resonance (LSPR) amplified fluorescence signal from the AuNRs to the QDs. The objective of this work is to develop a new fluorescent aptasensor for As (III) with improved analytical sensitivity and versatility. The developed Amp-P-AuFeZnSe QDs-AuNR fluorescence aptasensor was successfully applied for the detection of As (III) in environmental (river water) and biological (blood) samples. To the best of our knowledge, this is the first reported Amp-P-AuFeZnSe QDs-AuNR fluorescence aptasensor for As (III).

2. Materials and methods

2.1. Materials

Oleylamine, colbalt chloride hexahydrate, trioctylyphosphine oxide (TOPO), trioctylyphosphine (TOP), hexadecylamine (HDA), silver nitrate ($AgNO_3$), oleic acid, octadecene, selenium (Se),

sulphur, Trizma® acetate, N,N-diisopropylethylamine, poly(isobutylene-*alt*-maleic anhydride) and As (III) oxide were purchased from Merck. Citric acid and CTAB were purchased from Acros Organics. Myristic acid, *n*-octylamine, MES, indium chloride hydrate ($InCl_3.H2_O$), potassium phosphate monobasic ($KHPO_4$), potassium phosphate dibasic (KH_2PO_4), zinc acetate dihydrate ($ZnAc.2H_2O$), mercury (II) chloride, iron (II) chloride hexahydrate ($FeCl_3.6H_2O$), gold (III) chloride trihydrate ($HAuCl_4.3H_2O$), calcium chloride, silver nitrate ($AgNO_3$), and copper (II) chloride dihydrate were purchased from Thermo Fisher. All other chemicals were used as received. Anti As (III)-Apt with the sequence:
GGTAATACGACTCACTATAGGGAGATACCAGCTTATTCAATTTTACAGAACAACCAACGTCGC
TCCGGGTACTTCTTCATCGAGATAGTAAGTGCAATCT **[33]**, was synthesized and purified by Merck.

2.2. Characterization

Ultraviolet/visible (UV/vis) absorption and fluorescence emission measurements were carried out using a Varian Cary Eclipse spectrophotometer. Transmission electron microscopy (TEM) analysis were carried using a JEOL JEM-1200EX operated at 80 kV. X-ray Diffraction (XRD) analysis was carried out using a Siemens D5000 diffractometer with Cu Kα radiation (λ = 1.54056 nm) and data were obtained in the range of 3-90° using a 0.1° 2θ step size and a 3 sec count time per step with a 0.066° slit width. Dynamic light scattering (DLS) was carried out using a Zetasizer Nano ZS series (ZEN3600, Malvern).

2.3. Preparation of metal precursors

Iron oleate was synthesized according to previously reported procedure but with slight modification **[34]**. Briefly, 5.4 g $FeCl_3.6H_2O$ and 18.3 g sodium oleate were mixed with 40 mL ethanol, 70 mL hexane, and 30 mL MilliQ H_2O. The mixture was then stirred vigorously under N_2 gas for ~3 hours (hr) and 40 minutes (min) with moderate heat (between 60-80 ^oC) and was purified using acetone, acetone:chloroform, ethanol:acetone, and finally with acetone.

To prepare the TOPSe precursor, 0.12 g of Se was mixed with 5 mL of TOP **[35]**.

To prepare HDA-capped Au nanoparticle (AuNPs) used in the synthesis of the QDs, citrate-capped AuNPs were first synthesized according to previously reported procedure as follows **[35]**: 1 mL of 1% $HAuCl_4.3H_2O$ was mixed with ~79 mL of MilliQ H_2O, then, a mixture of 4 mL 1% trisodium citrate, 0.5 mL 1% tannic acid and 15.5 mL MilliQ H_2O was added into the Au solution. This resulted in the formation of AuNPs within few seconds as evidence from the formed reddish solution colour. The solution was heated to ~65 ^oC and stirred vigorously under ambient condition for ~15 min. To convert the hydrophilic citrate-AuNPs to hydrophobic HDA-AuNPs, 2 g of HDA was mixed with 25 mL toluene and the solution was sonicated to aid complete dissolution of the HDA ligand. Approximately, 50 mL of citrate-AuNPs was then added into the HDA-toluene solution and stirred for few seconds. The

solution was allowed to settle to aid separation of the organic HDA-AuNPs from the aqueous solution. HDA-AuNPs were carefully pipetted out of solution and stored in a vial.

2.4. Synthesis of Amp-P

Amp-P was synthesized according to previously published method but with slight modification **[36]**. In a three-necked flask, a mixture of 10 g poly(isobutylene-alt-maleic anhydride), 3 mL *n*-octylamine, 5.5 mL N,N-diisopropylethylamine, and 200 mL of chloroform was heated up (to ~65 ^{o}C) and stirred under ambient temperature for ~3 hr 40 min. Formation of the polymer network was evidenced from the increase in the viscosity of the solution. The polymeric solution was allowed to cool to room temperature and purified using acetone-ethanol mixture and finally with acetone. The purified product was dried in a fume hood and obtained as a fine powder.

2.5. Synthesis of AuFeZnSe QDs

AuFeZnSe QDs were newly synthesized via the organometallic hot-injection pyrolysis of metal precursors popularly used for the synthesis of Group II–VI QDs **[35]**. In a three-necked flask fitted with a reflux condenser, 0.4 g iron oleate, 0.9 g TOPO, 0.6 g Et_2Zn, 5 mL HDA-AuNPs, 0.6 g myristic acid, 5 mL of oleylamine, 20 mL of oleic acid, and 30 mL of octadecene were mixed together and stirred under heat and N_2 atmosphere. When the temperature of the solution reached ~245^{o}C, 3 mL of TOPSe solution was added into the AuFeZn precursor solution to initiate the nucleation and growth of AuFeZnSe alloyed QDs. The AuFeZnSe QDs was allowed to grow for 15 min and the reaction was stopped and allowed to cool to room temperature. The hydrophobic AuFeZnSe QDs were purified via centrifugation using acetone, ethanol:acetone, acetone, H_2O:chloroform:acetone:ethanol, and finally with acetone. The QDs product was dried in a fume hood and obtained as a fine orange powder.

2.6. Preparation of Amp-P-coated AuFeZnSe QDs

To overcoat the surface of hydrophobic AuFeZnSe QDs with Amp-P with the aim of rendering the QDs hydrophilic, 0.35 g AuFeZnSe QDs were dissolved in 20 mL chloroform and added into a polymeric-KOH-methanolic solution containing 3 g KOH, 40 mL methanol, and 0.4 g Amp-P. Appropriate volume of ultrapure MilliQ water was added into the solution and the solution was stirred for ~2 hrs 35 min. Purification of the QDs was carried via centrifugation using acetone and dried in a fume hood. A brownish-red fine crystalline QDs powder was obtained.

2.7. Synthesis of CTAB-AuNRs

The synthesis of CTAB-AuNRs was carried out using an established procedure where a seed solution was used to grow the rod-shaped NPs. The seed solution was prepared by mixing 5 mL of 2.5×10^{-3} M $HAuCl_4.3H_2O$, 10 mL of 0.1 M CTAB and ice-cold 0.6 mL of 0.1 M $NaBH_4$ in a vial. The solution was then gently swirled without no vigorous stirring so as to preserve the shape of the

nanoparticles during growth. The growth solution was prepared by gently mixing 5 mL of 2.5 × 10^{-3} M $HAuCl_4.3H_2O$, 10 mL of 0.1 M CTAB, 0.5 mL of 0.004 M $AgNO_3$, and 0.4 mL of 0.1 M ascorbic acid. Thereafter, 24 µL of the seed solution was added into the growth solution and the solution was swirled gently and allowed to stand still for ~20 hr. The CTAB-AuNR solution was mixed with appropriate volume of MilliQ H_2O and stored at ambient temperature before use.

2.8. Fluorescence assay

The buffer solution used in the fluorescence assay was prepared by mixing 2 g MES + 2 g Trisma acetate + 5 g KH_2PO_4 + 5 g K_2HPO_4 in 500 mL of MilliQ H_2O and the pH was adjusted to 7. The calculation of the AuNR concentration used in the fluorescence assay is provided in the Supplementary Information file. To prepare the fluorescence biosensor assay for As (III), 0.8 mg/mL Amp-P-AuFeZnSe QDs and 28 nM AuNRs (aspect ratio 2.8) were mixed electrostatically in a 1:1 (v/v) ratio to form an Amp-P-AuFeZnSe QDs-AuNR nanocomposite. Then, 175 µL of the Amp-P-AuFeZnSe QDs-AuNR was mixed with 10 µL of the anti-As(III) thiolated aptamer and 175 µL of targeted As (III) concentration (prepared in MES-Trisma acetate-KH_2PO_4-K_2HPO_4 pH 7 buffer). The solution was stirred, and the fluorescence emission spectrum was measured after ~15 seconds using a fluorescence spectrophotometer at an excitation wavelength of 200 nm within the fluorescence wavelength range of 210 - 800 nm.

3. Results and discussion

3.1. Fabrication of the Amp-P-AuFeZnSe alloyed QDs

Quaternary AuFeZnSe alloyed QDs were synthesized via the organometallic hot-injection route and stabilized with coordinating organic ligands as depicted in Scheme 1. In this work, HDA, myristic acid, oleylamine and oleic acid were used as organic surface stabilizing agents to render the QDs colloidally stable. The metal components of the QDs consisted of Au, Fe, Zn and Se, respectively. To generate the Au precursor, hydrophilic citrate-capped AuNPs were first synthesized and then converted to hydrophobic AuNPs via ligand exchange reaction of HDA in toluene. Rather than using the Fe salt directly in the QDs synthesis which could lead to unreacted Fe products, we synthesized Fe oleate and used it as the Fe precursor. This led to the complete dissolution of the Fe salt for the efficient nucleation and growth of the QDs. Zn and Se precursors were prepared and used as reported previously in the literature **[35]**. HDA-AuNPs and the other organic ligands used in the synthesis can be deoxygenated by the phosphonic precursors to yield anhydride products **[35].** As shown in Fig. S1, the UV/vis absorption spectrum of HDA-AuNPs used in the QDs synthesis was not red-shifted in comparison to the native citrate-AuNPs. This evidently shows that the HDA-AuNPs were not aggregated upon the ligand exchange reaction.

In order to render the QDs biocompatible and stable, Amp-P synthesized via a nucleophilic agent (*n*-octylamine) and an anhydride functionalized polymer backbone (poly(isobutylene-alt-maleic anhydride) (Mw = 6000 g/mol)) was used as the surface capping agent. The selected ratio between

the hydrophilic and hydrophobic units was derived by finetuning the relative number of organic-phased n-octylamine reactive groups. Relatively, 40% of anchored *n*-octylamine repeating units that is illustrated as 'm' in the schematic diagram of the polymer structure in Scheme 1, was used in the synthesis of the polymer. The fabricated method for the polymer synthesis provided the following advantages: (i) the ability to control the relative number of functional unit for effective polymer coating; (ii) the lack of a cross linker during the synthesis; (iii) effective control of the *n*-octylamine hydrophobic chains and also over the hydrophilic/hydrophobic formation of the polymer coating and (iv) the lack of a carbodiimide coupling reaction step for the QDs polymer coating.

3.2. Structural properties

SEM image of the Amp-P-AuFeZnSe alloyed QDs is shown in Fig. 1A. From the SEM monograph, the morphology of the Amp-P-QD nanocrystals was characterised by a porous honeycomb like heterostructure. The individual particles are interconnected, dense and stacked together with coarse honeycomb pores extending across the image surface. The corresponding TEM image shown in Fig. 1B depicts a heterostructure like morphology with some of the less stacked particles displaying quasi-like spherical shapes. From the TEM image, it is clearly evident that the Amp-P-QDs was characterized by a heterogeneous growth pattern.

The seed-mediated approach was successfully used to synthesize AuNRs. In this work, gold solution and weak reducing agents such as ascorbic acid and CTAB were used to grow the particles into nanorods. As shown in the TEM image of Fig. 1C, moderately short AuNRs with length of ~24 nm was clearly seen alongside some individual quasi-shaped spherical particles. Although, a mixture of rod-shaped and spherical shaped particles was formed, the rod-shaped particles were still more than the quasi-shaped spherical particles. The corresponding TEM image of the Amp-P-QDs-AuNR nanocomposite shown in Fig. 1D revealed a combination of individual rod-shaped particles and quasi-shaped spherical particles. The ability to observe individual rod-shaped particles in the Amp-P-QDs-AuNR nanocomposite structure, indicates that the morphology of the AuNRs was not distorted in the hybrid nanostructure.

PXRD pattern of the Amp-P-AuFeZnSe alloyed QDs is shown in Fig. 2A. From the diffraction pattern, three prominent peaks of {111}, {220} and {311} planes at 27.2 °, 45.6 °, and 54.4 ° were clearly projected. This evidently showed that the Amp-P-QDs exhibited a zinc-blende crystal structure similar to those notably observed for the diffraction pattern of other types of QDs chalcogenides **[36,37]**.

3.3. Optical properties

3.3.1. DLS and zeta potential analysis

DLS analysis was used to characterize the hydrodynamic size and to assess the degree of dispersity of the nanomaterials in solution. Fig. 2B-D shows the DLS histogram plots of CTAB-AuNRs, Amp-P-AuFeZnSe QDs, and the Amp-P-AuFeZnSe QDs-AuNR nanocomposite. For the AuNRs, the

hydrodynamic size was 18 nm while for the Amp-P-QDs and the Amp-P-QDs-AuNR, the hydrodynamic size were 408 nm and 64 nm respectively. Generally, hydrodynamic size >100 nm is indicative of polydispersed particles in solution while hydrodynamic size <100 nm is indicative of monodispersed particles in solution. For the AuNRs, the hydrodynamic size distribution was less than 100 nm and clearly shows that the particles were monodispersed in solution. Conversely, the hydrodynamic particles size of the Amp-P-QDs was greater than 100 nm, implying that the Amp-P-QDs were polydispersed in solution. The polydispersity could have been induced by the coating of the bulky polymer molecules. Interestingly, the hydrodynamic size of the Amp-P-QDs-AuNR nanocomposite was less than 100 nm, thus confirming the monodisperse nature of the particles in solution. The dramatic decrease in the hydrodynamic size of the Amp-P-QDs-AuNR relative to the Amp-P-QDs is indicative of the strong electrostatic binding interaction of the AuNRs with the Amp-P-QDs.

Zeta potential on the other hand was used to characterize the colloidal stability and surface charge of the nanomaterials in solution. Generally, the colloidal stability of NPs in solution are characterized according to: ±30 mV as highly stable, ±20-30 mV as moderately stable, ±10-20 mV as relatively stable and ±0-10 mV as highly unstable **[38].** This guideline was used in this work to assess the colloidal stability of the respective nanomaterials. Fig. S2A – C shows the zeta potential plots of CTAB-AuNRs, Amp-P-AuFeZnSe QDs, and the Amp-P-AuFeZnSe QDs-AuNR nanocomposite. From the plots, the zeta potential surface charge for CTAB-AuNRs was +57 mV, Amp-P-AuFeZnSe QDs was -12 mV and Amp-P-AuFeZnSe QDs-AuNR nanocomposite was +33 mV. From our analysis, the AuNRs were highly stable while the Amp-P-QDs were relatively stable. Our analysis also confirmed the positive charge of the AuNRs and the negative charge of the Amp-P-QDs and the obtained results were used as a means to establish the electrostatic interaction between the two nanomaterials. Interestingly, we observed that the Amp-P-QDs-AuNR nanocomposite surface charge was positive and within the range of highly stable colloidal dispersion. It is therefore imperative to suggest that the electrostatic interaction between the Amp-P-QDs and AuNRs did not distort the geometry of the plasmonic NP in solution. Rather, CTAB-AuNRs stabilized the Amp-P-QDs surface in the nanocomposite colloidal formation as evidenced by the highly stable surface charge value.

3.3.2. FT-IR analysis

FT-IR analysis of the Amp-P, AuNRs, Amp-P-QDs and the Amp-P-QDs-AuNR nanocomposite was carried out as shown in the displayed spectra of Fig. 2E. For the Amp-P, the band at 1771 cm^{-1} was ascribed to the C=O stretching vibration band while the band at 2966 cm^{-1} was attributed to the C-H stretching vibration. For the Amp-P-QDs, the band at 3310 cm^{-1} was assigned to the -OH stretching vibration while the bands at 2900 cm^{-1} and 1536 cm^{-1} were attributed to the C-H and COO asymmetric stretching vibration, respectively. For CTAB-AuNRs, the bands at 1647 cm^{-1} and 3196 cm^{-1} were assigned to the C=C stretching and N-H stretching vibrations. For the Amp-P-QDs-AuNR

nanocomposite, the bands at 3304 cm^{-1}, 2927 cm^{-1} and 1562 cm^{-1} were assigned to the N-H stretching, C-H stretching and COO asymmetric stretching vibration, respectively. From the obtained data, the C-H and COO stretching vibrations of the Amp-P-QDs-AuNR shifted to high wavenumber relative to the Amp-P-QDs while the N-H stretching band also shifted to higher wavenumber relative to the CTAB-AuNRs. Therefore, we can use the observed shift in projected bands of the Amp-P-QDs-AuNR nanocomposite as a means to confirm the established electrostatic interaction.

3.3.3. UV/vis absorption and fluorescence emission analysis

Fig. 3A shows the UV/vis absorption and fluorescence emission spectra of the synthesized quaternary Amp-P-QDs measured in MilliQ H_2O. The Amp-P-QDs was characterized by a broad UV/vis absorption spectrum with a less pronounced excitonic absorption peak around 378 nm. The fluorescence emission spectrum was projected at an emission wavelength maximum of 485 nm. For CTAB-AuNRs, the absorption spectrum shown in Fig. 3B, was characterized by two prominent SPR absorption peaks. The peak at 533 nm is attributed to the transverse absorption cross section of the NP which corresponds to the embedded spherical-shaped particles. On the other hand, the peak at 687 nm relates to the longitudinal cross section of the NP and it is attributed to the rod-shaped particles. Despite the presence of the transverse absorption peak, the TEM image of the NP shown in Fig. 1C, revealed the presence of more rod-shaped particles than spherical shaped particles with the ratio of rod-shaped particles to spherical particles being 1.6:1. Therefore, we have connoted the particles as being rod-shaped. The aspect ratio and the concentration of AuNRs were determined according to standard reported procedure **[39]** and the calculated procedure is provided in the Supplementary Information section. From our analysis, the calculated aspect ratio of the AuNRs was 2.8 while the concentration used in the fluorescence assay was 28 nM.

3.4. LSPR enhanced fluorescence intensity signal for As (III)

In order to prove the LSPR enhanced fluorescence signal of the Amp-P-Apt-QDs-AuNR hybrid nanocomposite for As (III), we carried out a series of comparative studies. As shown in Fig. 3C, the fluorescence of the Amp-P-QDs was quenched upon electrostatic interaction with the AuNRs, thereby switching OFF the fluorescence of the bound Amp-P-QDs. Immobilization of the Apt on the Amp-P-QDs-AuNR surface led to slight quenching of the bound Amp-P-QDs fluorescence with negligible effect. This proves to show that the Apt did not switch on the fluorescence of the bound Amp-P-QDs. Detection of 100 µg/L As (III) using the Amp-P-Apt-QDs triggered a slight enhancement in the fluorescence signal which corresponded to 12% increase in fluorescence intensity. Whereas, when the Amp-P-Apt-QDs-AuNR nanocomposite probe was used to detect the same concentration of As (III), the fluorescence of the bound Amp-P-QDs was enhanced by ~230%. This represented ~20-fold increase in fluorescence intensity over the Amp-P-Apt-QDs (without AuNRs). To confirm if the Apt-As (III) affinity binding influenced the LSPR amplified fluorescence intensity signal, the Amp-P-QDs-AuNR nanocomposite was interacted directly with As (III) without the presence of the Apt in

the system. As shown in Fig. 3C, the fluorescence spectrum of the Amp-P-QDs-AuNR for As (III) was quenched relative to the fluorescence response of the Amp-P-Apt-QDs-AuNR for As (III) recognition. Therefore, it is justifiable to conclude that LSPR from AuNR greatly amplified the fluorescence of the bound Amp-P-QDs upon As (III)-Apt binding, leading to a fluorescence turn ON signal effect for ultrasensitive As (III) recognition.

The reaction process underpinning the interaction of photon-emitting fluorophores with noble metal plasmonic NPs have long been reported in the literature **[40,41]**. Plasmonic metal NPs are known to act as either radiative fluorescence enhancers ("ON" state) or non-radiative fluorescence quenchers ("OFF" state) based on their size, shape and distance-dependent relationship with the fluorophore in an acceptor-donor interaction **[42].** The competition between fluorescence enhancement intensity and quenching effect is attributed to the electric field magnitude and dielectric dispersion of the nanomaterial at the particle surface which triggers either plasmon-amplified fluorescence enhancement for bigger-sized NPs or plasmon-mediated fluorescence quenching for smaller NPs **[42]**. Lakowicz simulation using the radiative plasmon theory showed that depending on the coupling effect between the SPR oscillation of the metal NP and the fluorophore at a close distance to the metal surface, the plasmon-amplified radiative fluorescence intensity enhancement ("ON" state) is induced by the cross section scattering of the NP, while the plasmon mediated non-radiative fluorescence quenching ("OFF" state) is triggered by the cross-section absorption of the NP **[40]**. Hence, we can deduce that the "OFF/ON" phenomena of the Amp-P-Apt-QDs-AuNRs aptasensor is triggered by the nature of the NP chemical environment, i.e., the fluorescence "OFF" state occurred with no Apt-As (III) binding interaction while the fluorescence "ON" state occurred with the Apt-As (III) binding interaction.

3.5. Mechanism of the fluorescence "OFF-ON" aptasensor assay

Scheme 1 shows the descriptive reaction mechanism of the Amp-P-Apt-QDs-AuNR biosensor probe for As (III). Firstly, the AuFeZnSe alloyed QDs was synthesized in the organic phase and surface-coated with organic ligands. Thereafter, the hydrophobic QDs was transformed to hydrophilic QDs via a robust Amp-P coating. CTAB-AuNRs was then electrostatically bonded to the Amp-P-QDs surface to form an Amp-P-QDs-AuNR hybrid nanocomposite. The binding interaction between CTAB-AuNPs and the Amp-P-QDs switched OFF radiative electron and hole recombination state in the fluorescence of the bound Amp-P-QDs. The thiol modified anti-As (III) DNA Apt was then immobilized on the Amp-P-QDs-AuNR nanocomposite surface by direct adsorption. The Apt could directly adsorb on the Amp-P-QDs-AuNR nanocomposite surface by either binding to the Amp-P-QDs, AuNR or both of the nanomaterial's surface without the use of a crosslinker. As shown in Fig. 3C, adsorption of the Apt on the Amp-P-QDs-AuNR nanocomposite surface did not switch on the fluorescence of the QDs. However, when the targeted As (III) was interacted with the Amp-P-Apt-QDs-AuNR probe, the immobilized Apt bonded strongly to the target As (III) analyte based on biomolecular affinity binding interactions. The binding interaction then triggered LSPR signal from

the bound AuNRs to amplify the fluorescence intensity signal of the bound Amp-P-QDs. Hence, radiation exciton recombination state in the bound Amp-P-QDs was switched ON with high sensitivity for As (III).

LSPR amplified fluorescence signals of QDs have been reported previously in the literature **[43,44]**. However, this is the first report on the use of LSPR amplified fluorescence signal from AuNRs to amplify the fluorescence intensity signal of newly synthesized Amp-P-AuFeZnSe QDs. Hence, we have plotted the fluorescence emission spectrum of the Amp-P-QDs against the absorption spectrum of the AuNRs as a means to unravel the theoretical basis for the LSPR induced fluorescence enhancement signal. As shown in Fig. 4A, the fluorescence emission spectrum of the Amp-P-QDs overlapped effectively with the absorption spectrum of the AuNRs. Therefore, the fluorescence quenching of the Amp-P-QDs could occur via nano-metal surface energy transfer (NSET) as previously reported for QDs-AuNP interaction **[44]**. Despite the spectral overlap, Förster resonance energy transfer mechanism could not have been the mode of interaction because both the Amp-P-QDs fluorescence and the AuNR absorption were each quenched relative to their unbound state as shown in Fig. 4A. Therefore, we have predicted NSET as the binding mode of interaction between the Amp-P-QDs and AuNRs.

In general, Apt are known to fold into various secondary forms such as stem, loop, bugle, pseudo-knot, and G-quadruplex, which in effect allows the Apt to molecularly recognize their target by forming a three-dimensional (3D) structure **[45]**. The Apt is then able to bind to the target in a 3D manner via either of hydrogen bonding, shape complementarity, base stacking, van der Waals forces, hydrophobic or electrostatic interactions **[46].** Since the target As(III) is a heavy metal, the suggested mode of binding interaction between by the Apt is likely electrostatic interaction, hydrogen bonding or van der Waals forces. According to Kim et al., prediction of the structural analysis of the Apt-As binding using Zuker's algorithm Mfold, showed that the Apt exhibited hairpin loop architecture which can be classified into branched and tight secondary structure **[47]**. It was also further reported that As binds to the regions of the hairpin, base-pairing, or hairpin loop structures of the Apt **[47]**.

3.6. Optimization of the fluorescence aptasensor assay

Several experimental analysis were carried out to optimize the fluorescence aptasensor assay for As (III) recognition. Fig. 4B shows the fluorescence spectra and corresponding turn ON intensity signal (inset) studied from pH 6-11 for As (III) recognition using the Amp-P-Apt-QDs-AuNR biosensor probe. From the data, the fluorescence intensity signal increased from pH 6 to 7 and then decreased steadily as the pH increased to pH 9 and thereafter increased as the pH reached pH 11. In general, optimum fluorescence intensity signal was obtained at pH 7 and was chosen as the choice pH for the Amp-P-Apt-QDs-AuNR aptasensor As (III) assay.

The effect of the Amp-P-QDs concentration from 0.1 – 0.8 mg/mL for As (III) detection was studied. The Amp-P-Apt-QDs-AuNR biosensor assay was prepared with different Amp-P-QDs concentration at a fixed concentration of the Apt (1 µM) and the AuNRs (28 µM). As shown in Fig. 5A, the effect of

the Amp-P-QDs concentration on the fluorescence intensity signal did not follow a definite trend. The corresponding effect of the Amp-P-QDs concentration on the UV/vis absorption spectra of the Amp-P-QDs-AuNR nanocomposite is also shown in Fig. S3A. It was observed that as the concentration of the Amp-P-QDs decreased, the transverse SPR absorption peak became clearly visible in the absorption spectra as the concentration of the Amp-P-QDs decreased. However, the intensity of the SPR peak did not also follow a symmetric trend with respect to the tested Amp-P-QDs concentration. Hence, it is imperative to conclude that the fluorescence intensity signal for As (III) recognition was specific for each tested Amp-P-QDs concentration. Relative to the control, optimum fluorescence intensity signal was obtained for 0.8 mg/mL Amp-P-QDs concentration, and this was chosen as the choice concentration for the Amp-P-Apt-QDs-AuNR aptasensor As (III) assay.

The effect of the LSPR amplified fluorescence intensity signal was studied by varying the Amp-P-QDs to AuNRs ratio for As (III) detection. By fixing the Amp-P-QDs and AuNR concentration at 0.8 mg/mL and 28 µM respectively, the Amp-P-QDs to AuNR v/v ratio was studied from 1:1 to 1:5. As shown in Fig. 5B, the LSPR amplified fluorescence intensity signal of the Amp-P-Apt-QDs-AuNR biosensor probe towards As (III) decreased as the Amp-P-QDs to AuNR v/v ratio increased. The corresponding UV/vis absorption spectra (Fig. S3B) showed that as the Amp-P-QDs to AuNR v/v ratio increased, the SPR absorption transverse and longitudinal peak became stronger. Based on our results, the Amp-P-QDs to AuNR 1:1 v/v ratio which produced the highest fluorescence intensity signal, was selected as the choice ratio for the As (III) fluorescence biosensor assay.

3.7. Selectivity of the fluorescence aptasensor assay

The selectivity of the fluorescence turn ON aptasensor assay for As (III) using the Amp-P-Apt-QDs-AuNR biosensor probe was studied. Several metal cations known to be present in the environment were tested under the same experimental conditions as As (III). Fig. 6 shows the fluorescence intensity signal generated for 14 tested metal cations in comparison to As (III). We have also tested As (V) and probed the generated fluorescence response in comparison to fluorescence response of the targeted As (III). As shown in the data, the fluorescence turn ON signal for As (III) was far superior than the signal generated from all tested metal cations. Slight enhancement in fluorescence signal was observed for some of the tested metal cations. However, the signal generated for As (III) was at least 2-fold or more higher than the signal generated for these cations. This implies that none of the tested metal cations generated significant fluorescence turn ON effect in comparison to the signal generated for As (III). It is also important to emphasize that the fluorescence signal generated for As (V) was far lower than the signal generated for the targeted As (III). This implies that the developed Amp-P-Apt-QDs-AuNR fluorescence aptasensor probe can discriminate efficiently between As (III) and As (V) based on the clear difference in fluorescence responses. Based on our results, it is imperative to say that the developed Amp-P-Apt-QDs-AuNR biosensor probe was highly selective to As (III).

3.8. Quantitative As (III) detection

Ultrasensitive quantitative detection of As (III) from 0.01 – 100 µg/L was carried using the developed Amp-P-Apt-QDs-AuNR biosensor probe. As shown in Fig. 7A, the fluorescence emission spectra of the developed Amp-P-Apt-QDs-AuNR probe were steadily enhanced as increased concentration of As (III) was detected. The most remarkable observation was that a total of 230% fluorescence intensity increase was obtained at 100 µg/L detected As (III) concentration. The corresponding fluorescence intensity calibration curve for quantitative As (III) detection is shown in Fig. 7B. From the plot, the limit of detection (LOD) was calculated by multiplying the standard deviation of blank measurement (n = 10) by three and dividing by the slope of the fluorescence signal calibration plot while the limit of quantitation (LOQ) was determined by multiplying the obtained LOD by 3.3. The LOD obtained for As (III) using the Amp-P-Apt-QDs-AuNR biosensor probe was 0.01 µg/L (69.12 pM) and it was 1000 times lower that the WHO permissible LOD recommended for As **[1]**. The calculated LOQ was 0.03 µg/L.

3.9. Real sample application

The application of the Amp-P-Apt-QDs-AuNR probe to detect As (III) in real samples (biological and environmental) was investigated. Cow blood samples collected locally from an abattoir in Perth, Scotland, (with ethical permission) and river water collected locally from the River Tay in Monifieth, Dundee, were both spiked with 0.5, 0.1 and 0.05 µg/L concentrations of As (III). As shown in Table 1, the spiked As (III) concentrations were detected successfully in both cow blood and river water with satisfactory recoveries in the range of ~ 93-105%. Hence, we can affirm that the Amp-P-Apt-QDs-AuNR biosensor probe is efficiently suitable to detect As (III) in biological and environmental samples. Comparative data showing the analytical performance of the Amp-P-Apt-QDs-AuNR probe for As (III) with other published methods is listed in Table 2. The comparison shows that our detection system is more sensitive and versatile to detect ultralow concentration of As (III) in both environmental samples (river sample) and biological samples (blood) than the published probes for these sample types. Also, the comparison of our QDs fluorophore probe with other QDs published probes, showed that our detection system is more environmentally friendly as it does not contain the toxic cadmium ion.

4. Conclusions

We have successfully constructed a novel fluorescence OFF-ON apatsensor for As (III). Quaternary Amp-P-AuFeZnSe alloyed QDs were newly synthesized and electrostatically bonded to cationic AuNRs to form an Amp-P-AuFeZnSe QDs-AuNR hybrid nanocomposite. The Amp-P-QDs, AuNRs and the Amp-P-QDs-AuNR nanomaterials were characterized using electron microscopy and optical spectroscopic techniques. The binding interaction between the Amp-P-QDs and AuNR, switched OFF the fluorescence of the bound QDs. By assembling the thiolated anti-As (III) Apt on the Amp-P-QDs-AuNR surface, As (III) was able to bind to the Apt receptor with high affinity. The binding

interaction between the Apt and As (III) on the Amp-P-QDs-AuNR surface, triggered LSPR signal from AuNR to amplify the fluorescence intensity signal of the bound Amp-P-QDs. We observed that the presence of AuNRs in the nanocomposite structure, amplified the fluorescence intensity signal of the bound Amp-P-QDs by 230%, representing an ~20-fold increase over the Amp-P-Apt-QDs probe without AuNRs. As (III) was selectively and quantitatively detected with ultra-high sensitivity with the detection limit being 1000 times more sensitive than the WHO recommended limit for As. Application of the Amp-P-Apt-QDs-AuNR probe to detect As (III) in environmental (river water) and biological (blood) samples was successfully achieved.

Acknowledgements

Authors gratefully acknowledge the financial support from Leverhulme Trust for funding this work. OA sincerely appreciates the support received from the School of Science and Engineering, University of Dundee.

Appendix A. Supporting information

Supplementary data associated with this article can be found in the online version at doi:

References

1. A.A. Meharg, A. Raab, Getting to the Bottom of Arsenic Standards and Guidelines, Environ. Sci. Technol. 44 (2010) 4395–4399.
2. B.K. Mandal, K.T. Suzuki, Arsenic round the world: a review, Talanta 58 (2002) 201-235.
3. W.R. Cullen, K.J. Reimer, Arsenic speciation in the environment, Chem. Rev. 89 (1989) 713-764.
4. H. Kaur, R. Kumar, J.N. Babu, S. Mittal, Advances in arsenic biosensor development– a comprehensive review, Biosens. Bioelectron. 63 (2015) 533-545.
5. D. Banik, S.K. Manna, A.K. Mahapatra, Recent development of chromogenic and fluorogenic chemosensors for the detection of arsenic species: Environmental and biological applications, Spectrochim. Acta A Mol. Biomol. Spectrosc. 246 (2021) 119047.
6. A. Basu, D. Saha, R. Saha, T. Ghosh, B. Saha, A review on sources, toxicity and remediation technologies for removing arsenic from drinking water, Res. Chem. Intermed. 40 (2014) 447-485.
7. K. Ohnishi, H. Yoshida, K. Shigeno, S. Nakamura, S. Fujisawa, K. Naito, K. Shinjo, Y. Fujita, H. Matsui, A. Takeshita, S. Sugiyama, H. Satoh, H. Terada, R. Ohno, Prolongation of the QT interval and ventricular tachycardia in patients treated with arsenic trioxide for acute promyelocytic leukemia, Ann. Intern. Med. 133 (2000) 881-885.
8. V.K. Gupta, A. Nayak, S. Agarwal, R. Dobhal, D.P. Uniyal, P. Singh, B. Sharma, S. Tyagi, R. Singh, Arsenic speciation analysis and remediation techniques in drinking water, Desalin. Water Treat. 40 (2012) 231-243.

9. B. Sadee, M.E. Foulkes, S.J. Hill, Coupled techniques for arsenic speciation in food and drinking water: a review, J. Anal. At. Spectrom. 30 (2015) 102-118.
10. T.M. Clancy, K.F. Hayes, L. Raskin, Arsenic waste management: a critical review of testing and disposal of arsenic-bearing solid wastes generated during arsenic removal from drinking water, Environ. Sci. Technol. 47 (2013) 10799-10812.
11. R.K. Zalups, D.J. Koropatnick, Molecular Biology and Toxicology of Metals. CRC Press, Taylor and Francis Group (2000).
12. X.-Y. Yu, T. Luo, Y. Jia, Y.-X. Zhang, J.-H. Liu, X.-J. Huang, Porous hierarchically micro-/nanostructured MgO:morphology control and their excellent performance in As(III) and As(V) removal, J. Phys. Chem. C 115 (2011) 22242-22250.
13. E. Munoz, S. Palmero, Analysis and speciation of arsenic by stripping potentiometry: a review, Talanta. 65 (2005) 613-620.
14. M. Asadollahzadeh, N. Niksirat, H. Tavakoli, A. Hemmati, P. Rahdari, M. Mohammadi, R. Fazaeli, Application of multi-factorial experimental design to successfully model and optimize inorganic arsenic speciation in environmental water samples by ultrasound assisted emulsification of solidified floating organic drop microextraction, Anal. Methods 6 (2014) 2973-2981.
15. M. Vahter, Metabolism of arsenic, in: B.A. Fowler (Ed.), Biological and Environmental Effects of Arsenic. Elsevier, Amsterdam, (1983) pp. 171–198.
16. P.B. Tchounwou, A.K. Patlolla, J.A. Centeno, Carcinogenic and systemic health effects associated with arsenic exposure – a critical review, Toxicol. Pathol. 31 (2003) 575-588.
17. J. Das, P. Sarkar, A new dipstick colorimetric sensor for detection of arsenate in drinking water, Environ. Sci. Water Res. Technol. 2 (2016) 693–704.
18. Y. Xiao, J. Ling, S. Qian, A. Lin, W. Zheng, Y. Xu, Y. Luo, M. Zhang, Preconcentration of trace arsenite and arsenate with titanium dioxide nanoparticles and subsequent determination by silver diethyldithiocarbamate spectrophotometric method, Water Environ. Res. 79 (2007) 1015–1022.
19. E. Bralatei, K. Nekrosiute, J. Ronan, A. Raab, E. McGovern, D.B. Stengel, E.M. Krupp, J. Feldmann, A field deployable method for a rapid screening analysis of inorganic arsenic in seaweed, Microchim. Acta 184 (2017) 1701–1709.
20. X. Xu, X. Niu, X. Li, Z. Li, D. Du, Y. Lin, Nanomaterial-based sensors and biosensors for enhanced inorganic arsenic detection: A functional perspective, Sens. Actuators B Chem. 315 (2020) 128100.
21. A.A. Ensafi, N. Kazemifard, B. Rezaei, A simple and sensitive fluorimetric aptasensor for the ultrasensitive detection of arsenic(III) based on cysteamine stabilized CdTe/ZnS quantum dots aggregation, Biosens. Bioelectron. 77 (2016) 499–504.
22. F. Divsar, K. Habibzadeh, S. Shariati, M. Shahriarinour, Aptamer conjugated silver nanoparticles for the colorimetric detection of arsenic ions using response surface methodology, Anal. Methods 7 (2015) 4568–4576.

23. L. Farzin, M. Shamsipur, S. Sheibani, A review: Aptamer-based analytical strategies using the nanomaterials for environmental and human monitoring of toxic heavy metals, Talanta 174 (2017) 619–627.
24. K. Mao, H. Zhang, Z. Wang, H. Cao, K. Zhang, X. Li, Z. Yang, Nanomaterial-based aptamer sensors for arsenic detection, Biosens. Bioelectron. 148 (2020) 111785.
25. Y. Li, L. Sun, Q. Zhao, Aptamer-structure switch coupled with horseradish peroxidase labeling on a microplate for the sensitive detection of small molecules, Anal. Chem. 91 (2019) 2615–2619.
26. S. Zhan, Y. Wu, L. Wang, X. Zhan, P. Zhou, A mini-review on functional nucleic acids-based heavy metal ion detection, Biosens. Bioelectron. 86 (2016) 353–368.
27. J. Li, X. Hu, S. Shi, Y. Zhang, T. Yao, Three label-free thrombin aptasensors based on aptamers and $[Ru(bpy)_2(\sigma\text{-mopip})]^{2+}$, J. Mater. Chem. B 4 (2016) 1361–1367.
28. S. Centi, S. Tombelli, M. Minunni, M. Mascini, Aptamer-based detection of plasma proteins by an electrochemical assay coupled to magnetic beads, Anal. Chem. 79 (2007) 1466–1473.
29. W. Li, S. Wang, L. Zhou, Y. Cheng, J. Fang, An ssDNA aptamer selected by Cell-SELEX for the targeted imaging of poorly differentiated gastric cancer tissue, Talanta 199 (2019) 634–642.
30. H. Du, X. Wang, Q. Yang, W. Wu, Quantum dot: Lightning invisible foodborne pathogens, Trends Food Sci. Technol. 110 (2021) 1–12.
31. S. Thakkar, L.F. Dumée, M. Gupta, B.R. Singh, W. Yang, Nano–Enabled sensors for detection of arsenic in water, Water Res. 188 (2021) 116538.
32. S.K. Vaishanav, J. Karram, P. Pradham, K. Chandraker, R. Nagwanshi, K.K. Ghosh, M.L. Satnami, Green luminescent CdTe quantum dot based fluorescence nano-sensor for sensitive detection of arsenic (III), J Fluoresc, 27 (2017) 781–789.
33. T. Mushiana, N. Mabuba, A.O. Idris, G.M. Peleyeju, B.O. Orimolade, D. Nkosi, R.F. Ajayi, O.A., Arotiba An aptasensor for arsenic on a carbon-gold bi-nanoparticle platform, Sens. Bio-Sens. 24 (2019) 100280.
34. L.M. Armijo, Y.I. Brandt, D. Mathew, S. Yadav, S. Maestas, A.C. Rivera, N.C. Cook, N.J. Withers, G.A. Smolyakov, N.L. Adolphi, T.C. Monson, D.L. Huber, H.D.C. Smyth, M. Osiński, Iron oxide nanocrystals for magnetic hyperthermia applications, Nanomaterials 2 (2012) 134-146.
35. O. Adegoke, K. Takemura, E.Y. Park, Plasmonic oleylamine-capped gold and silver nanoparticle-assisted synthesis of luminescent alloyed CdZnSeS quantum dots, ACS Omega 3 (2018) 1357−1366.
36. S. Saleem, S. Rangou, C. Abetz, B. Lademann, V. Filiz, V. Abetz, Block copolymer membranes from polystyrene-b-poly(solketal methacrylate) (PS-b-PSMA) and amphiphilic polystyrene-b-poly(glyceryl methacrylate) (PS-b-PGMA), Polymers 9 (2017) 216.
37. O. Adegoke, T. Nyokong, Probing the sensitive and selective luminescent detection of peroxynitrite using thiol-capped CdTe and CdTe@ZnS quantum dots, J. Lumin. 134 (2013), 448-455.

38. V. Uskoković, Z. Castiglione, P. Cubas, L. Zhu, W. Li, S. Habelitz, Zeta-potential and particle size analysis of human amelogenins, J. Dent. Res. 89 (2010) 149–153.
39. S. Biswas, P. Tripathi, N. Kumar, S. Nara, Gold nanorods as peroxidase mimetics and its application for colorimetric biosensing of malathion, Sens. Actuators B Chem. 231 (2016) 584-592.
40. J.R. Lakowicz, Radiative decay engineering 5: metal-enhanced fluorescence and plasmon emission, Anal. Biochem. 337 (2005) 171–194.
41. K.H. Drexhage, Influence of a dielectric interface on fluorescence decay time, J. Luminesc. 1.2 (1970) 693–701.
42. T. Pons, I.L. Medintz, K.E. Sapsford, S. Higashiya, A.F. Grimes, D.S. English, H. Mattoussi, On the quenching of semiconductor quantum dot photoluminescence by proximal gold nanoparticles, Nano Lett. 7 (2007) 3157–3164.
43. F. Nasrin, A.D. Chowdhury, K. Takemura, I. Kozaki, H. Honda, O. Adegoke, E.Y. Park, Fluorometric virus detection platform using quantum dots-gold nanocomposites optimizing the linker length variation, Anal. Chim. Acta. 1109 (2020) 148-157.
44. M.A. Pereira-Barros, N. Nic Daeid, O. Adegoke, Rapid and selective aptamer-based fluorescence detection of salivary lysozyme using plasmonic metal-enhanced fluorescence of ZnSSe alloyed quantum dots-gold nanoparticle nanohybrid, J. Photochem. Photobiol. A: Chem. 418 (2021) 113384.
45. J. Zhou, J. Rossi, Aptamers as targeted therapeutics: current potential and challenges, Nat. Rev. Drug Discov. 16 (2017) 181–202.
46. A.D. Gelinas, D.R. Davies, N. Janjic, Embracing proteins: structural themes in aptamer–protein complexes, Curr. Opin. Struct. Biol. 36 (2016) 122–132.
47. M. Kim, H.-J. Um, S. Bang, S.-H. Lee, S.-J. Oh, J.-H. Han, K.-W. Kim, J. Min, Y.-H. Kim, Arsenic Removal from vietnamese groundwater using the arsenic-binding DNA aptamer, Environ. Sci. Technol. 43 (2009) 9335–9340
48. V.C. Ezeh, T.C. Harrop, Synthesis and properties of arsenic(III)-reactive coumarin-appended benzothiazolines: a new approach for inorganic arsenic detection, Inorg. Chem. 52 (2013) 2323-2234.
49. D. Ghosh, M.N. Luwang, Arsenic detection in water: $YPO_4:Eu^{3+}$ nanoparticles, J. Solid State Chem. 232 (2015) 83-90.
50. S. Lohar, S. Pal, B. Sen, M. Mukherjee, S. Banerjee, P. Chattopadhyay, Selective and sensitive turn-on chemosensor for arsenite ion at the ppb level in aqueous media applicable in cell staining, Anal. Chem. 86 (2014) 11357-11361.
51. C. de Villiers, M. Lapsley, E. Hall, A step towards mobile arsenic measurement for surface waters, Analyst 140 (2015) 2644-2655.

52. S.K. Vaishanav, J. Korram, P. Pradhan, K. Chandraker, R. Nagwanshi, K.K. Ghosh, M.L. Satnami, Green luminescent CdTe quantum dot based fluorescence nano-sensor for sensitive detection of arsenic (III), J. Fluoresc. 27 (2017) 781-789.
53. J. Wang, H. Tao, T. Lu, Y. Wu, Adsorption enhanced the oxidase-mimicking catalytic activity of octahedral-shape Mn_3O_4 nanoparticles as a novel colorimetric chemosensor for ultrasensitive and selective detection of arsenic, J. Colloid Interface Sci. 584 (2021) 114–124.
54. Y.G. Wu, S.S. Zhan, F.Z. Wang, L. He, W.T. Zhi, P. Zhou, Cationic polymers and aptamers mediated aggregation of gold nanoparticles for the colorimetric detection of arsenic(III) in aqueous solution, Chem. Commun. 48 (2012) 4459–4461.
55. Y.G. Wu, L. Liu, S.S. Zhan, F.Z. Wang, P. Zhou, Ultrasensitive aptamer biosensor for arsenic(III) detection in aqueous solution based on surfactant-induced aggregation of gold nanoparticles, Analyst 137 (2012) 4171–4178.
56. S. Banerjee, N.P. Kumar, A. Srinivas, S. Roy, Core-shell Fe_3O_4@Au nanocomposite as dual-functional optical probe and potential removal system for arsenic (III) from Water, J. Hazard. Mater. 375 (2019) 216–223.
57. S.H. Wen, Y. Wang, Y.H. Yuan, R.P. Liang, J.D. Qiu Electrochemical sensor for arsenite detection using graphene oxide assisted generation of Prussian blue nanoparticles as enhanced signal label, Anal. Chim. Acta 1002 (2018) 82–89.
58. T. Gupte, S.K. Jana, J.S. Mohanty, P. Srikrishnarka, S. Mukherjee, T. Ahuja, C. Sudhakar, T. Thomas, T. Pradeep, Highly sensitive As^{3+} detection using electrodeposited nanostructured MnO_x and phase evolution of the active material during sensing. ACS Appl. Mater. Interfaces 11(2019) 28154–28163.

Table 1. Analytical parameters of the Amp-P-Apt-QDs-AuNR biosensor probe for As (III) detection in cow blood and river water.

Matrix	As (III), µg/L spiked	Found (µg/L)	Recovery (%)	RSD (%, n=3)
Cow blood	0.5	0.524	~104.9	8.4
Cow blood	0.1	0.096	~96.6	11.0
Cow blood	0.05	~0.048	~95.8	22.7
River water	0.5	~0.517	~103.4	13.4
River water	0.1	0.093	~93.1	8.3
River water	0.05	0.051	102.4	11.8

Table 2. Analytical performance of the Amp-P-Apt-QDs-AuNR biosensor probe for As (III) detection in comparison to other published methods.

Probe	Method	Concentration range	Applicable detection Matrix	LOD	Ref.
Coumarin-bonded benzothiazolines	Fluorescence	-	Water	0.1 µg/L	**48**
$YPO_4:Eu^{3+}$ NPs	Fluorescence	0-10 mg/L	Water	10 mg/L	**49**
Schiff triggered cell permeable receptor	Fluorescence	-	Water	4.12 µg/L	**50**
Glutathione-CdTe & CdSe/ZnS QDs	Fluorescence	2247 mg/L – 0.375 µg/L	River water	74.92 µg/L	**51**
L-cysteine capped CdTe QDs	Fluorescence	0.75–22.5 µg/L	Water	0.226 µg/L	**52**
Oxidase mimetic Mn_3O_4 NPs	Colorimetry	5-100 µg/L	Tap water, river water and wheat	1.32 µg/L	**53**
Cationic polymer-Apt-AuNPs	Colorimetry	5-100 µg/L	-	5.3 µg/L	**54**
Apt-CTAB-AuNPs	Colorimetry	1-100 µg/L	Water	0.6 µg/L	**55**
Fe_3O_4/Au NPs	Colorimetry	0-20 µg/L	Water	0.86 µg/L	**56**
Graphene oxide/Prussian blue NPs	Electrochemical	0.2-500 µg/L	Tap water, river water and lake water	0.058 µg/L	**57**
MnO_x	Electrochemical	1-150 µg/L	Water	1 µg/L	**58**
Amp-P-Apt-QDs-AuNR	Fluorescence	0.01-100 µg/L	Blood & river water	0.01 µg/L	This work

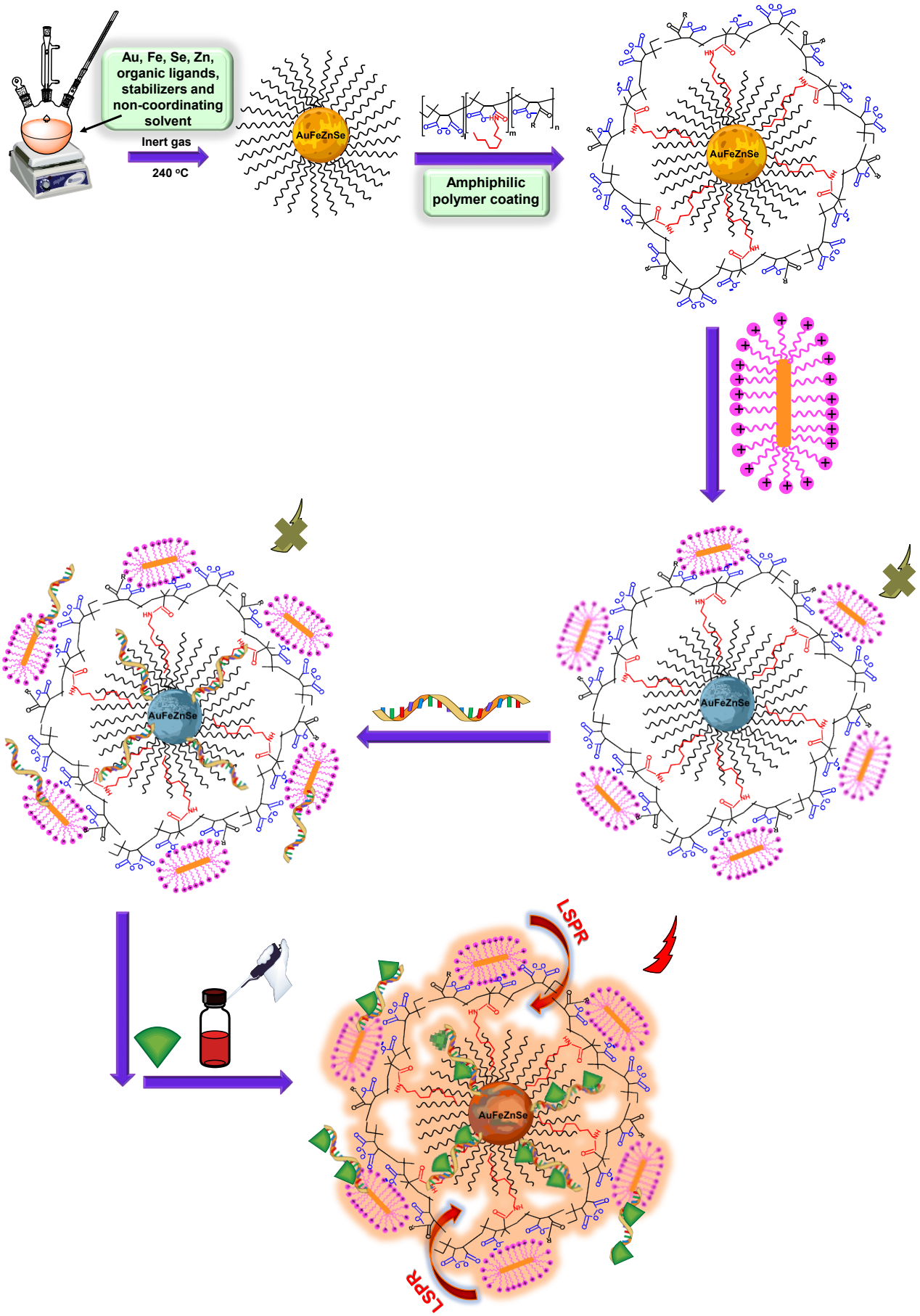
Au, Fe, Se, Zn, organic ligands, stabilizers and non-coordinating solvent
Inert gas
240 °C
AuFeZnSe
Amphiphilic polymer coating
AuFeZnSe
AuFeZnSe
AuFeZnSe
LSPR
LSPR
AuFeZnSe

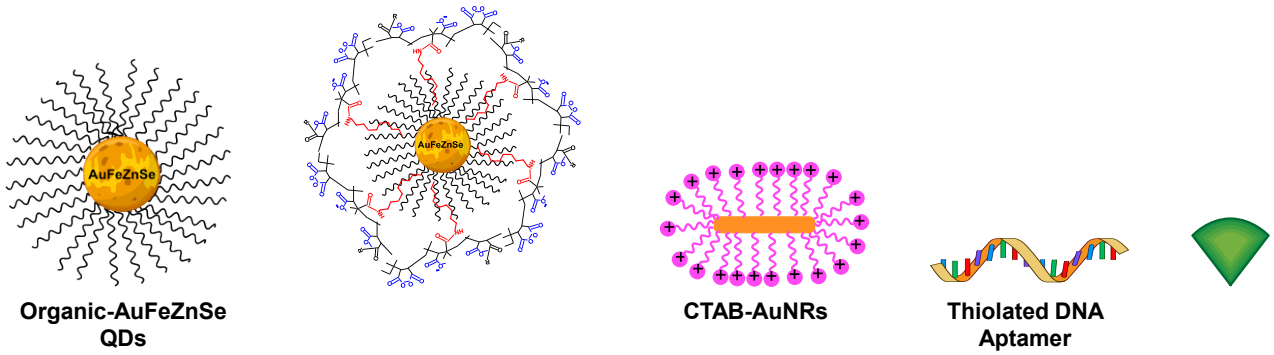

Scheme 1. Schematic representation of the Apt-Amp-P-QDs-AuNR fluorescence OFF-ON biosensor probe for As (III) recognition. Quaternary AuFeZnSe alloyed QDs is first synthesized in the organic phase and then coated with Amp-P to generate water-soluble and biocompatible Amp-P-coated AuFeZnSe QDs. The prepared Amp-P-AuFeZnSe QDs is then electrostatically bonded to cationic CTAB-AuNR to form an Amp-P-AuFeZnSe QDs-AuNR hybrid. The bonding resulted in the fluorescence of the bound Amp-P-QDs being switched OFF. Thiolated anti As (III) DNA Apt is then immobilized on the AuFeZnSe QDs-AuNR hybrid surface. In the presence of the targeted As (III) concentration, the Apt binds to As (III) which in turn switches ON the bound Amp-P-QDs fluorescence with high sensitivity via LSPR effect from AuNRs.

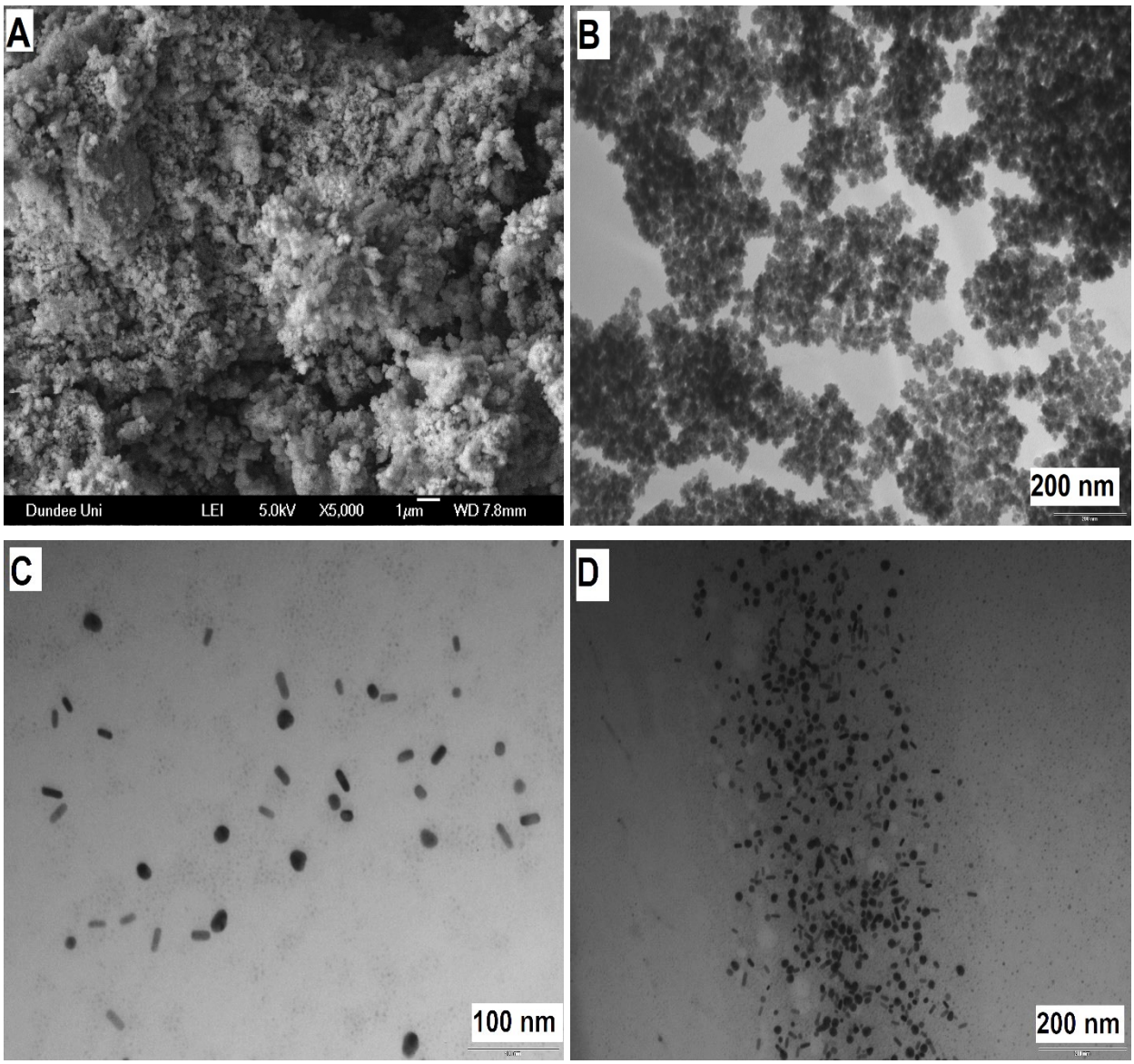

Fig. 1. SEM image of the (A) Amp-P-AuFeZnSe QDs, and TEM images of the (B) Amp-P-AuFeZnSe QDs, (C) CTAB-AuNRs, and the (D) Amp-P-AuFeZnSe QDs-AuNR hybrid nanostructure.

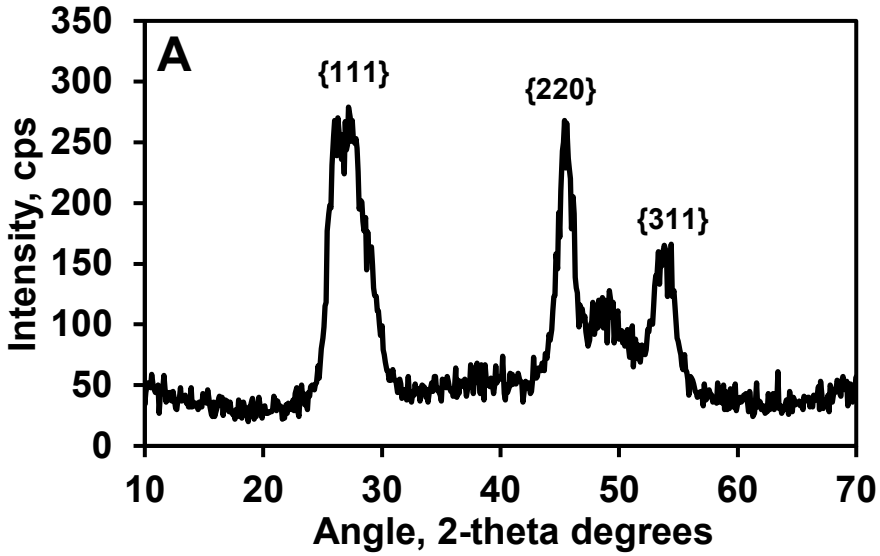
A
{111}
{220}
{311}
Intensity, cps
350
300
250
200
150
100
50
0
10
20
30
40
50
60
70
Angle, 2-theta degrees

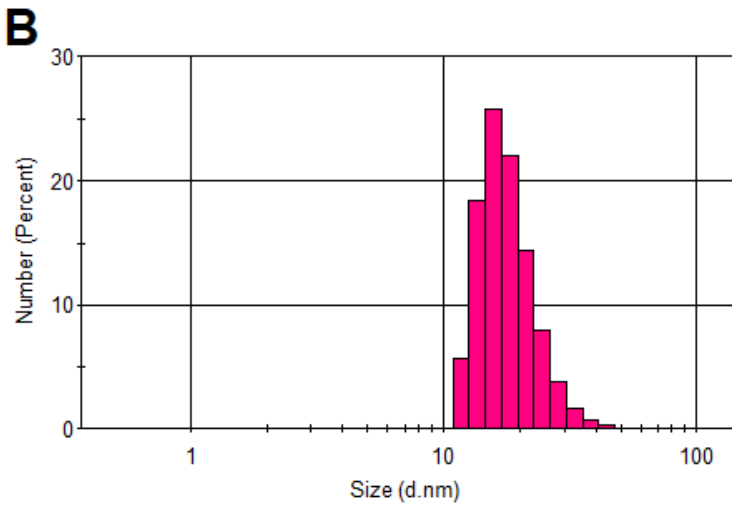
B
30
20
10
0
Number (Percent)
1
10
100
Size (d.nm)

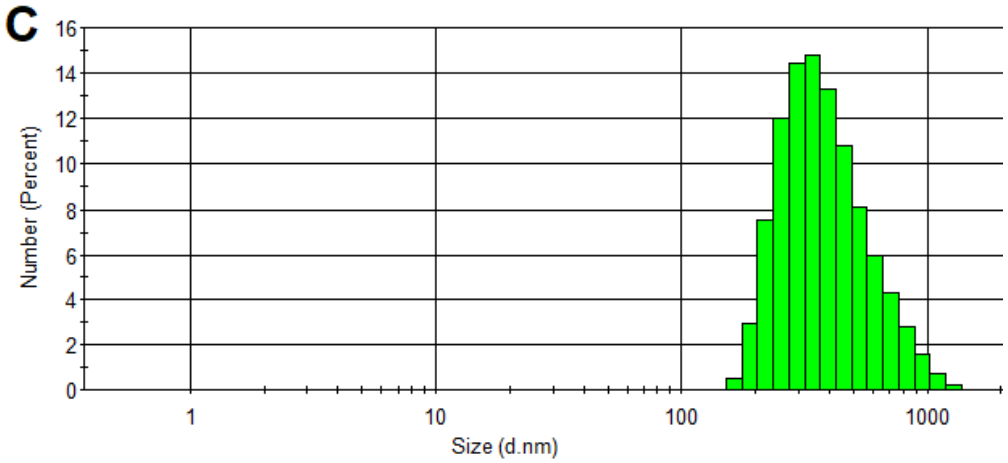
C
16
14
12
10
8
6
4
2
0
Number (Percent)
1
10
100
1000
Size (d.nm)

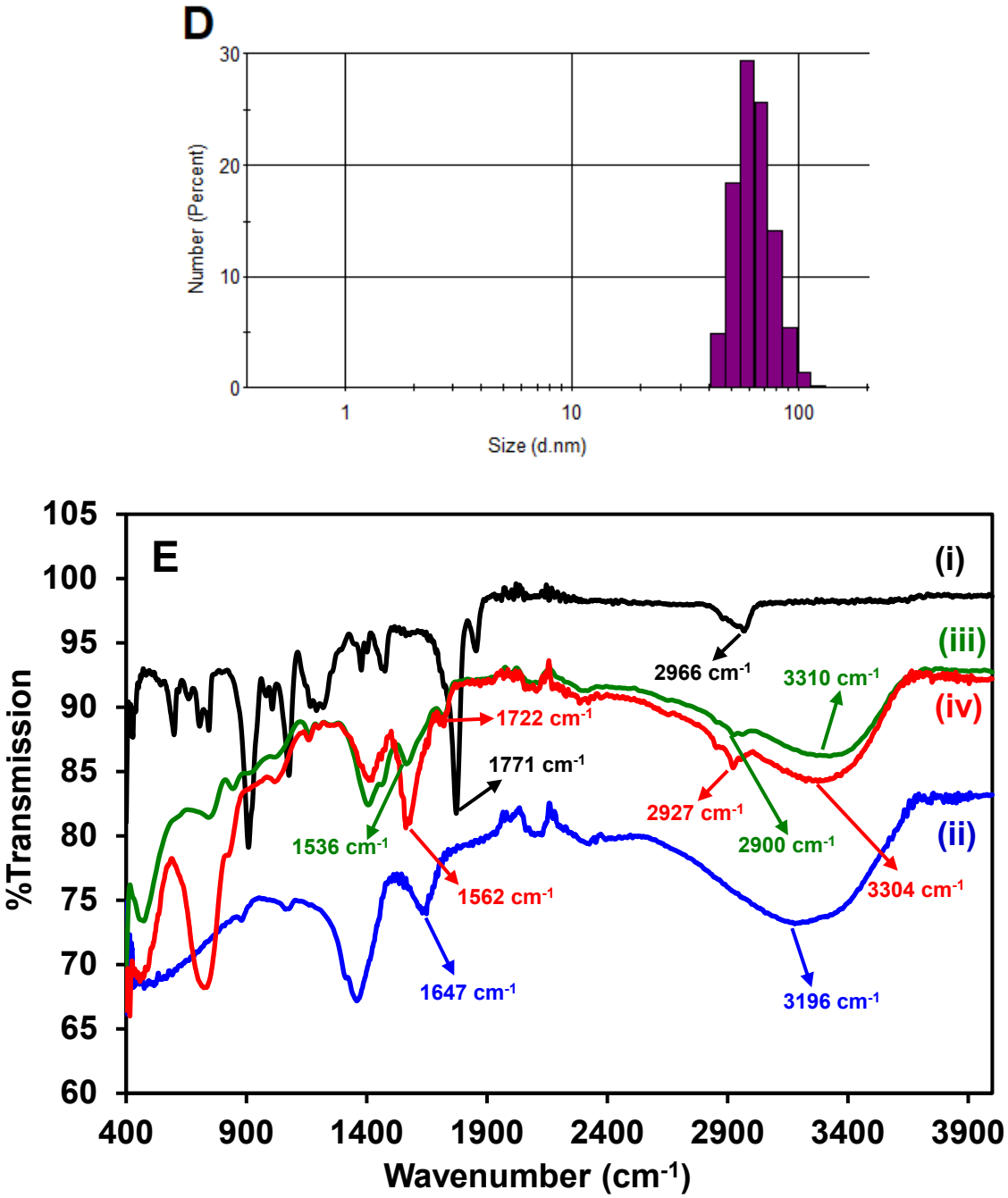

Fig. 2. (A) PXRD pattern of the Amp-P-AuFeZnSe QDs. DLS plots of the (B) CTAB-AuNRs, (C) Amp-P-AuFeZnSe QDs, and the (D) Amp-P-AuFeZnSe QDs-AuNR nanocomposite. (E) FT-IR spectra of the (i) Amp-P, (ii) AuNRs, (iii) Amp-P-QDs and the (iv) Amp-P-QDs-AuNR nanocomposite.

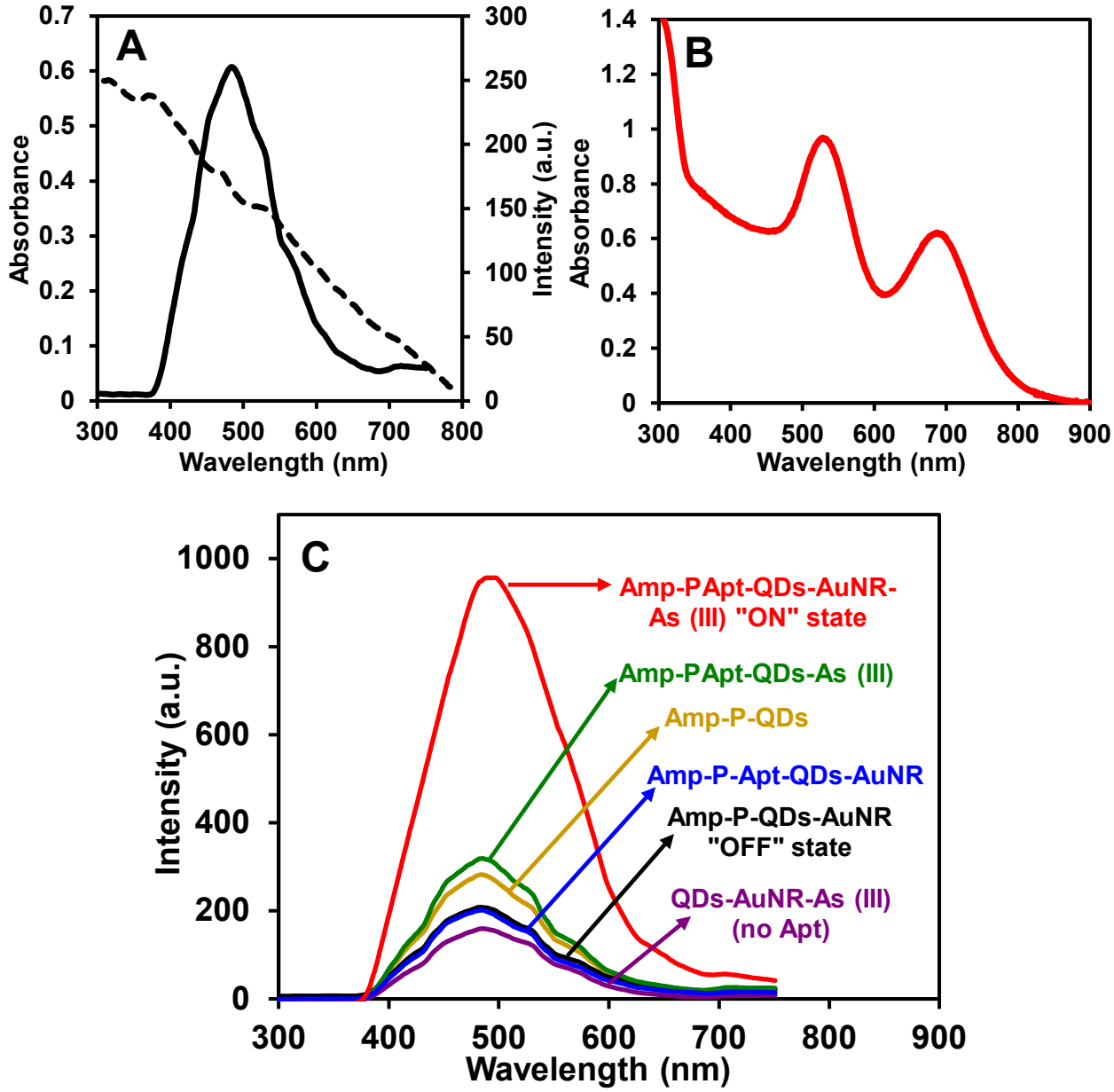

Fig. 3. (A) UV/vis (dotted line) and fluorescence emission spectra (solid line) of Amp-P-AuFeZnSe QDs. (B) UV/vis absorption spectrum of the CTAB-AuNRs and (C) comparative fluorescence emission spectra of the Amp-P-QDs, Amp-P-QDs-AuNR hybrid, Amp-P-Apt-QDs-AuNR, and the fluorescence spectra response for As (III) using the Amp-P-QDs-AuNR nanocomposite (no Apt), Amp-P-Apt-QDs and the Amp-P-Apt-QDs-AuNR nanocomposite. [As (III)] = 100 µg/L.

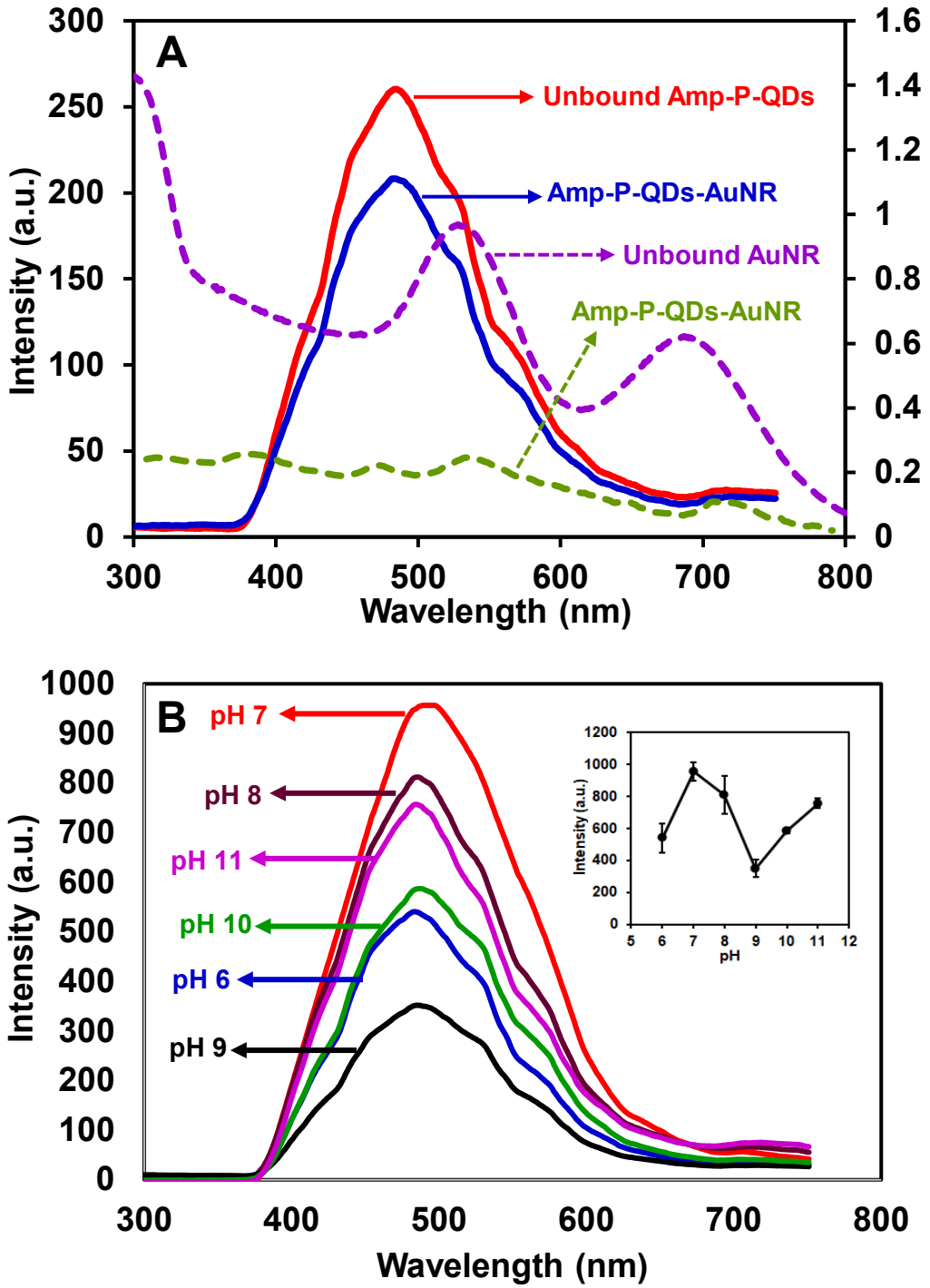

Fig. 4. (A) Spectral overlap between the fluorescence emission spectrum of the unbound Amp-P-AuFeZnSe QDs and the UV/vis absorption spectrum of the unbound CTAB-AuNRs. The fluorescence emission and UV/vis absorption spectra of the Amp-P QDs-AuNR hybrid is also shown. (B) Fluorescence spectra and corresponding intensity signal (inset) for As (III) detection (100 µg/L) at different pH using the Amp-P-Apt-QDs-AuNR hybrid nanocomposite biosensor probe.

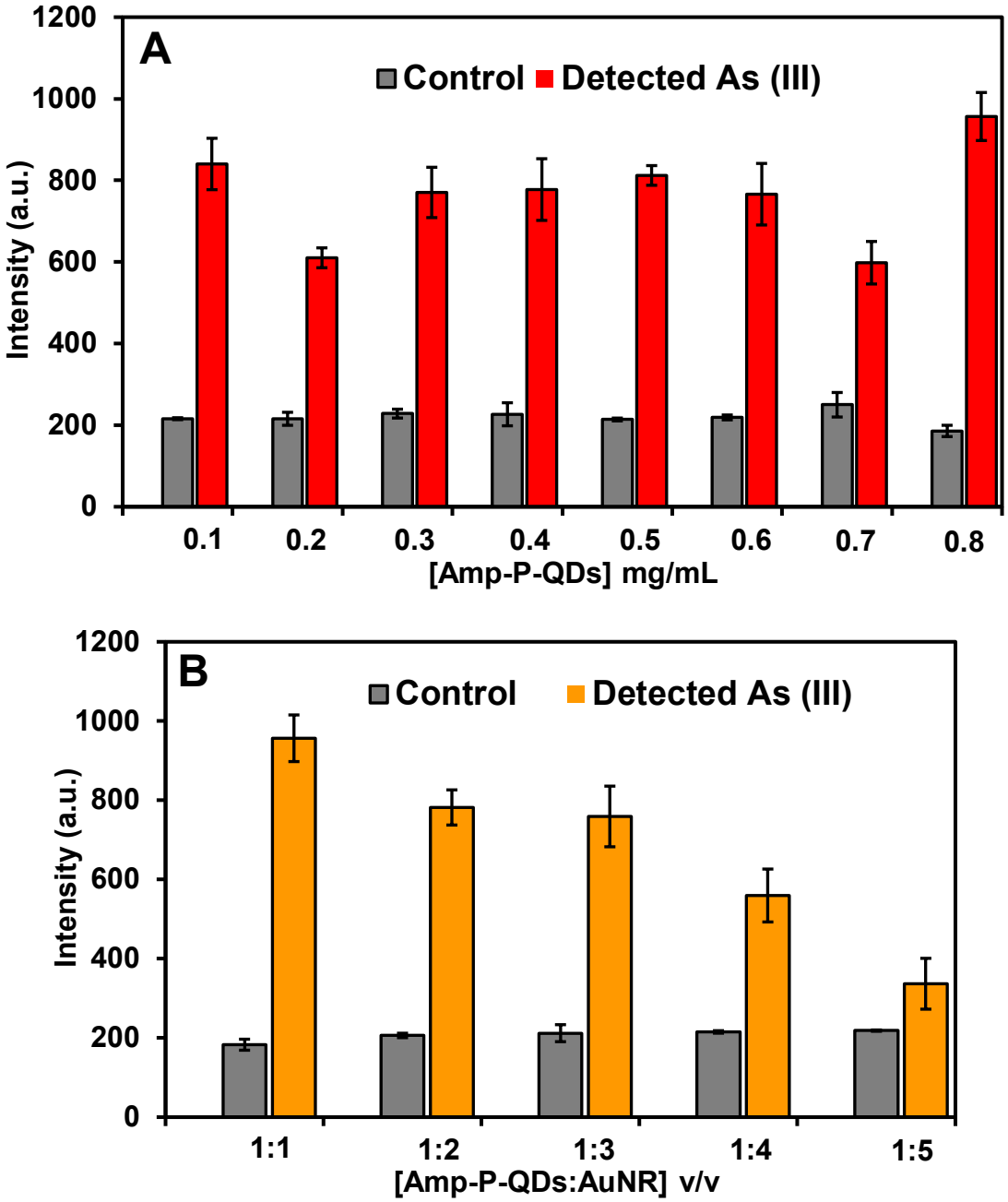

Fig. 5. LSPR fluorescence enhanced intensity signal showing (A) the effects of the Amp-P-QDs concentration for the detection of As (III) at a fixed AuNR concentration (28 nM) and the (B) effect of the Amp-P-QDs:AuNR v/v ratio for As (III) recognition. Control = Amp-P-QDs-AuNR. [Apt] = 1 μM.

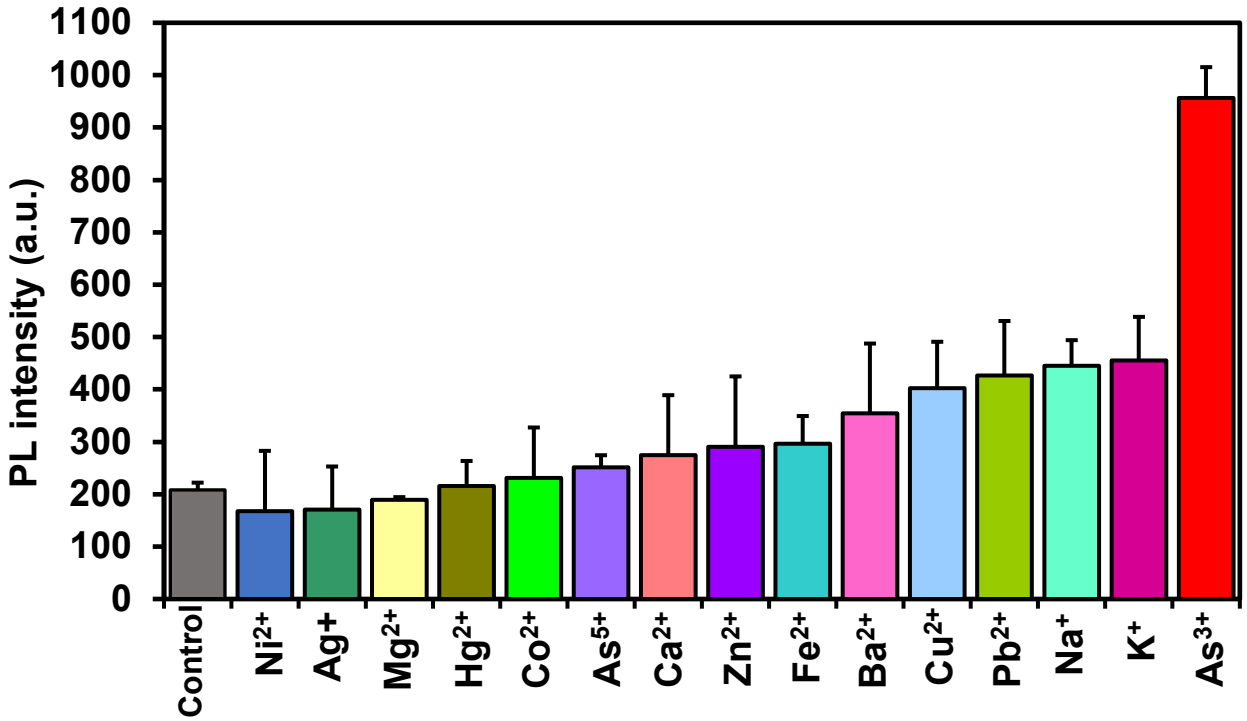

Fig. 6. LSPR fluorescence enhanced intensity signal showing the selectivity of the Amp-P-Apt-QDs-AuNR biosensor probe towards As (III) detection. All analyte concentration were fixed at 100 µg/L.

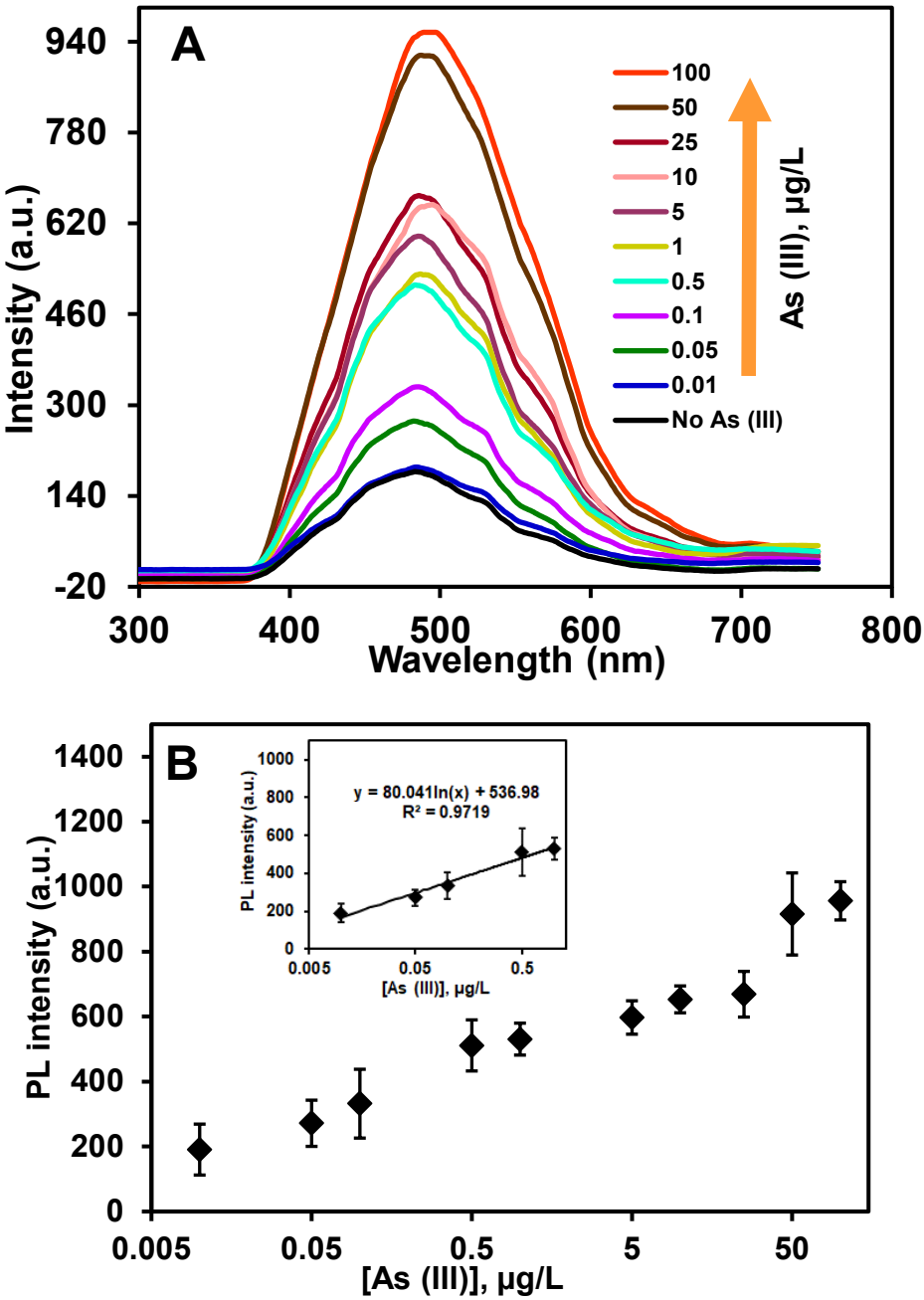

Fig. 7. (A) LSPR fluorescence enhanced spectra showing the quantitative detection of As (III) using the Amp-P-Apt-QDs-AuNR biosensor probe. (B) Corresponding fluorescence intensity signal plotted against each detected As (III) concentration in order to generate the calibration plot. Inset of Fig. 7B: Linear calibration plot.